DEUTSCHES ELEKTRONEN-SYNCHROTRON DESY

DESY SR-78/20
October 1978

USE OF SYNCHROTRON RADIATION IN X-RAY INTERFEROMETRY

by

G. Materlik

NOTKESTRASSE 85 · 2 HAMBURG 52

To be sure that your preprints are promptly included in the
HIGH ENERGY PHYSICS INDEX ,
send them to the following address (if possible by air mail) :

DESY
Bibliothek
Notkestrasse 85
2 Hamburg 52
Germany

Use of Synchrotron Radiation in X-ray Interferometry

G. MATERLIK
Deutsches Elektronen-Synchrotron DESY,
Notkestr. 85, D-2000 Hamburg 52, Germany

Abstract

Recently developed techniques to profitably utilize the special characteristics of synchrotron radiation in x-ray interferometry are described. The advantages of synchrotron x-ray when compared to interferometry with conventional and rotary anode x-ray tubes are discussed and outlined in two cases, namely x-ray dispersion spectroscopy and three-beam case interferometry.

1. Introduction

During the past five years the outstanding characteristics of synchrotron radiation found rapidly increasing application to problems in X-ray spectroscopy and X-ray diffraction. Among those were the first tests with X-ray interferometers by Bonse & Materlik (1975 a,b) who used DESY in Hamburg as radiation source and showed that the very high spectral and angular luminosity of this source, combined with the small emitted divergence, its wavelength tunability and the well defined polarization state harmonizes ideally with the small intrinsic angular acceptance of single crystals.

This experience led to the first continuous measurement of the anomalous dispersion correction on either side of an X-ray absorption edge (Materlik (1975), Bonse & Materlik (1976)) and to the first successful operation of a dispersive three-beam case X-ray interferometer (Graeff (1976), Graeff & Bonse (1977)).

The profitable utilization of synchrotron X-rays was in either case realized by specially adapting the interferometric setup to the properties of the synchrotron source which are quite different to those of conventionally used X-ray tubes. This difference made substantial changes of the goniometer arrangement necessary, like the use of a vertical reflection plane for the dispersion correction measurement. Besides this, new concepts had to be used to overcome problems just

caused by the nature of this radiation. For example, the elimination of higher Bragg reflected orders became essential. These appear because of the continuous wavelength distribution from the visible down to 0.1 Å γ-rays. Of course the high intensity also is responsible for a drastic increase in scattered radiation background and for a strong heat load on the first diffraction element which can exceed several Watts per cm^2.

The solution of these problems not only made it possible to carry out the above mentioned interferometer experiments, but also opens the way for several other studies of interferometer devices and interferometer applications. The easy accessibility of the short wavelength region below 0.5 Å allows to study, as in the case of neutrons, diffraction moirés from "thin" interferometers for which absorption is small and Pendellösungeffects become dominant. Diffraction focussing (Indenbom, Slobodetskii & Truni (1975)) can be investigated similar to the neutron case, furthermore, a well defined photon polarization state can be applied to reduce the number of excited wavefields and to study the polarization dependence of Pendellösungeffects for "thin" interferometers. The problem of X-ray resonators (Deslattes (1968)) and X-ray Fourier spectroscopy (Hart (1975)) may then also be experimentally attacked by making use of the high intensity and a suitable wavelength fit best for highly dispersive interferometer designs. This last property might also be a benefit for certain applications of interferometric phase contrast microscopy. The number of dispersive electrons can then be changed by tuning into an absorption edge.

It is therefore useful to describe the interferometer setup which was adapted to synchrotron X-rays and to discuss in detail in which way special source properties effected the arrangement and which methods were used to make full use of the wavelength tunability and of the angular collimation.

2. Interferometric setup for use with Synchrotron X-radiation

The diffractometer is shown schematically in Fig. 1 for two different angles of incidence Θ_1 and Θ_2. Also inserted are the respective beam paths. The stationary entrance slit is located about 30 m away from the tangent point of the electron orbit. The radiation is monochromatized by a grooved monochromator (or "channel cut") which fulfills several tasks. In the first place it cuts a very small wavelength region out of the white incident spectrum which is given by $\Delta\lambda/\lambda = \Delta\Theta \cot \Theta$. $\Delta\Theta$ is determined by the divergence coming from the source and is usually about 10^{-4} to 10^{-3} for each reflected order. The once diffracted beam therefore already has the monochromacy of a characteristic X-ray line or even better. Secondly, by closely shielding the crystal, as shown in the photograph Fig. 2, the radiation background can be suppressed because from the direction of the twofold reflected beam one can no more look directly on the spot where the primary beam is stopped by the first mirror. Thirdly, if the first Bragg mirror is heated by the intensive radiation, one can design the groove in such a way, that the relative angle between the Bragg mirrors can be changed by elastical deformation of a weak link cut in the base of the groove (Materlik & Kostroun (1978)). Since different d spacings for the first and second reflection shift the Θ position of the respective single crystal reflection ranges, this is then corrected by adjusting the Bragg angle for the second reflection, so that the overlap is again maximized.

The two interference beams, being generated by the LLL interferometer, respond quite different to a change of the Bragg angle Θ. As illustrated in Fig. 1, the rotation of the spectrometer by $\Delta\Theta$ results in a sweep of the H-beam across the stationary film while the O-beam, being redirected parallel to the primary beam, virtually stays at the same spatial position. In the case shown, Δs = 0.5 mm for $\Delta\Theta = 3^\circ$ and λ = 1.54 Å. This beam is therefore very well suited for use with detectors while the H-direction produces a wavelength scale on a film or on another

position sensitive device like a TV camera or position sensitive detector.

The fringe moiré of a wedge placed into one of the interference beams is displayed on the inset of Fig. 1. At the position λ_o a section pattern has been recorded. The wavelength resolution is then determined by the source divergence and the distance of the groove to the tangent point. In the region from λ_1 to λ_2 the diffractometer has been driven continuously and the resolution is thus also depending on the distance of the film to the interferometer and can be varied by this means.

The LLL interferometer is remotely adjustable parallel and perpendicular to the Laue mirrors and so are the three independent rotations $\Delta\theta$, $\Delta\rho$ and $\Delta\kappa$, where $\Delta\theta$ determines the relative alignment of groove and interferometer in the reflection plane. The remote control of all important parameters of the diffractometer is necessary because the whole experiment is interlocked while the synchrotron radiation beam is turned on.

As will be discussed in chapter 3 the polarization state and the higher collimation perpendicular to the orbital plane, which is not effected by the curvature of the orbit, require in many applications a vertical reflection plane. This means that all X-ray optical components have to be rigidly mounted without inducing any strains. The interferometer designed for this purpose is shown in Fig. 3. The deep groove in the base serves as an obstacle for lattice deformations from the glue which connects the interferometer base with a L-shaped silicon bloc. This bloc buffers the different thermal expansions of the silicon and the steel plate.

Also shown in Fig. 3 is the built-in moiré. The visible lattice dilatation with a fringe distance $\Lambda_D \approx 1$ mm is produced by a lattice constant variation $\Delta d/d = d/\Lambda_D \approx 2 \cdot 10^{-7}$. Presently it has not been investigated, whether this

dilatation is produced by different heating of the interferometer mirrors when they are hit by the intensive synchrotron radiation beam.

3. Polarization and angular collimation

One peculiarity of synchrotron X-rays is their polarization state. The normalized intensities of the radiation components with the electrical vector parallel ($P_{\parallel}$) and perpendicular ($P_{\perp}$) to the electron orbit are plotted in Fig. 4 a as a function of the angle Ψ to the horizontal plane. The width at half-maximum of $P_{\parallel}$ is about 0.16 mrad and reflects also the high collimation of the relativistically compressed radiation cone emitted by one electron. $P_{\perp}$ exhibits two maxima with a separation of 0.14 mrad. Both are much smaller in height than the maximum of $P_{\parallel}$. A very high degree of linear polarization is reached close to the orbital plane, while the polarization is elliptical if the accepting slit moves out of the plane. It becomes more and more circular for increasing Ψ (Kunz (1976)), because the phase difference between $P_{\parallel}$ and $P_{\perp}$ is $\pm \pi/2$ and the amplitudes are then almost equal.

The ideal case that all electrons are travelling along a central orbit is never fulfilled in an actual synchrotron or storage ring. There the electrons oscillate about a central orbit (betatron oscillations) in such a way, that for each cross-section of the beam the distance of an electron to the center of the bunch and the corresponding angular divergence are connected by an elliptical relation (Green (1975)). For the storage ring DORIS in Hamburg such phase space ellipse for an electron energy 3 GeV is shown in Fig. 4 b for the vertical beam distribution in direction $\vec{z}$ ($\vec{z}$ perpendicular to the orbit) and the divergence $z' = dz/ds$ where $\vec{s}$ is the unit vector parallel to the tangent and perpendicular to $\vec{z}$. The shape of the

ellipse varies along the orbit and depends on the actual accelerator beam optic. However, if the particle is only radially accelerating, the area of the ellipse is a constant of motion and the vertical and horizontal betatron oscillations can usually be treated independently.

Shown in Fig. 4 b is the curve representing the width at half-maximum of a normal density distribution for the electron beam. In this case the maximum divergence of the betatron oscillations is 0.38 mrad which is about twice the natural divergence of the synchrotron radiation at 1.5 Å photon wavelength. Of course this also changes the total degree of polarization reached within a receiving slit and a polarizer, as discussed at the end of this chapter, might become necessary.

The phase ellipse for the horizontal plane is usually larger than for the vertical and the smearing by the curvature of the ring has to be included also. Either fact supports a vertical reflection plane if the highest possible wavelength resolution for one single crystal diffraction shall be reached. The machine parameters which determine the phase ellipses can fortunately be specified for each beam optic and one can thus successfully treat the influence of the phase ellipse and of all slits placed into the beam to define the source portion used and the corresponding divergence (Green (1975), Hastings (1976), Pianetta & Lindau (1977)).

The proof of the high polarization and collimation of DESY and their dependence on the beam optic is given in Fig. 5. A wedge fringe system has been recorded using a horizontal reflection plane with the arrangement shown in Fig. 1. The diagrams are densitometer profiles along the traces indicated by the arrows. The intensity distribution of the perpendicularly polarized component $P_\perp$ (Fig. 4 a) is visible and the comparison of part a and b gives a contrast change which follows from an increase in source height. The separation of the two maxima in Fig. 5 a is about 0.14 mrad. This shows, that the divergence of the vertical

betatron oscillations is very small at that particular section of the orbit.

The use of the Laue mirror as a Borrmann polarizer (Cole, Chambers & Wood (1961)) makes this illustration possible. As is well-known the Borrmann effect strongly favours the wavefields with an electrical vector perpendicular to the reflection plane. The anomalous small absorption coefficient for an energy flow parallel to the net planes is in the two-beam case given by (Borrmann (1955))

$$\mu^{c}_{min} = \frac{\mu_o}{\cos \theta_B} \left(1 - C \left|\frac{\chi_{io}}{\chi_{ih}}\right|\right) \qquad (1)$$

where μ_o is the normal photoelectric absorption coefficient and χ_{io}, χ_{ih} are imaginary parts of the O, H-Fourier components of the electrical susceptibility. The polarization state ($C = 1$ for perpendicular and $C = |\cos 2\theta|$ for parallel polarization to the reflection plane) introduces the strong difference in absorption. This difference in the Laue case can be used to construct a simple polarizer. Only by this means, full use of the polarization of synchrotron X-rays can be made, specially if the influence of betatron oscillation is considered.

4. Continuous spectrum and higher orders

The easy wavelength tunability is another main advantage of synchrotron radiation. Fig. 6 shows the intensity distribution from DESY in a given entrance slit 29 m away from the source as a function of wavelength in the region $\lambda = 0.3$ Å to 3.0 Å. The available flux was compared to that from a Cu K_α line, generated by a 30 kW Rigaku Denki rotating anode (R) and by a conventional 1.5 kW sealed X-ray tube (C). The comparison was done by using the same setup (Fig. 1) in either case. The intensities were measured with films and normalized to the theoretical synchrotron radiation flux. As was pointed out in the last chapter, the source divergence determines the actual energy passband. In our experiment this parameter was not controlled which let to uncertainties in $\Delta\lambda/\lambda$ (marked by the bars for (R) and

(C)). A factor of about 10 can be gained when compared to (R)[+] and another factor 10 when compared to (C). But this comparison is done for the intensities of a characteristic X-ray line! When real tunability is wanted, like in dispersion spectrometry (Bonse & Materlik (1976)), conventional X-ray generators only offer the bremsspectrum. Here the comparable intensities are reduced by another factor 500 - 1000. It also has to be noted, that the increase in intensity and thus the decrease in exposure or counting time is in many cases not only of quantitative but also of qualitative nature, because the influence of thermal and vibrational disturbances is reduced.

The continuous spectrum extending far into the hard X-ray region, offers the advantage to test the interferometer for long and short wavelengths at the same Bragg angle. Thus one can carry out interferometry with varying absorption and extinction length up to the absorption free neutron-like case (Bauspieß, Bonse & Graeff (1976)). This became possible by the development of a new method to eliminate the harmonics which are always present(with the exception of forbidden reflections) after one single crystal reflection of a wide spectrum. The idea is to use the refractive index correction to the Bragg angle (Bonse & Materlik (1975 a)) which introduces a wavelength dependence of the angular position of the center of the reflection range. Besides this the center position is also coupled to the asymmetry factor $b = \sin(\phi + \theta)/\sin(\phi - \theta)$, where ϕ is the angle between the surface and the reflecting Bragg planes. It is (Zachariasen (1967))

$$\theta_o - \theta_B = (1 - \frac{1}{b}) \frac{|\chi_{ro}|}{2 \sin 2\theta_B} + \frac{|\chi_{rh}| C}{|b|^{1/2} \sin 2\theta_B} y \qquad (2)$$

and

$$\theta_h - \theta_B = -b\ (\theta_o - \theta_B) \qquad (3)$$

[+]The intensity of the rotating anode could be doubled for short periods of time. However, the chances of vacuum and power failures then increased remarkably for the model used.

$$\chi_{ro} = -\frac{r_e}{\pi} \frac{F_o}{V} \lambda^2 \ ; \ \chi_{rh} = -\frac{r_e}{\pi} \frac{F_h}{V} \lambda^2 \qquad (4)$$

Here θ_o, θ_h are the reflection angles for incidence and reflectance respectively, χ_{ro}, χ_{rh} are the real parts of the electrical susceptibility, connected to the structure factors F_o, F_h, r_e is the classical radius of the electron and V the volume of the unit cell. The parameter y gives the deviation from the center ($y = 0$) of the reflection range. The principle of this method has been discussed in detail by Bonse, Materlik & Schröder (1976), its application to monolithic monochromators by Materlik & Kostroun (1978).

Silicon 220 reflection curves for $\lambda = 1.54$ Å, and the higher orders $\lambda/2$ and $\lambda/3$ are shown in Fig. 7 for two polarization states presuming parallel incident plane waves. The centers of the λ and $\lambda/2$ reflection ranges are shifted by 3.1 seconds of arc. Since $b = 1$ in the symmetrical Laue case all curves are then centered at θ_B. The combination of a Bragg case groove and a Laue case interferometer as shown in Fig. 1 realizes a simple way to select harmonics by tuning the relative θ adjustment of the two optical components.

The wedge moirés in Fig. 8, photographed at each O position simultaneously in the H- and O-beam, exhibits the different fringe spacings for λ, $\lambda/2$ and $\lambda/3$ but furthermore the remarkable change of the reflex structure due to Pendellösung oscillations. For $\lambda = 1.5$ Å the interferometer is Borrmann-like ($\mu_o t \gtrsim 23$), for 0.75 Å ($\mu_o t \gtrsim 2.9$) a further modulation is introduced (different in H- and O-beam) perpendicular to the interferometer base which becomes even more pronounced for $\lambda = 0.5$ Å ($\mu_o t \gtrsim 0.9$).

5. Applications

As mentioned in the introduction the two fields in X-ray interferometry, which so far have profitted most from synchrotron radiation, are the measurement of the

dispersion correction f' close to X-ray absorption edges and the development of dispersive X-ray interferometers. The final chapter therefore explains which properties of synchrotron X-radiation and which of the above mentioned methods of adaption to the source characteristics were crucial to the before mentioned experiments.

5.1 Dispersion spectroscopy

The refractive index n of a homogeneous medium with N atoms per unit volume, and the coherent forward scattering amplitude $f = f_o + f' + if''$, are for X-rays connected by

$$1 - n = \frac{r_e}{2\pi} \lambda^2 N(f_o + f') \qquad (5)$$

n was measured on either side of the nickel K absorption edge by Bonse & Materlik (1976) with the setup sketched in Fig. 1 and the details of Fig. 2 and Fig. 3. A lucite wedge produced a fringe system which was shifted when the sample was inserted into an interference beam. The fringe system was photographed with and without sample and the relative shifts were determined with a digitizing densitometer and successive computer analysis. A vertical reflection plane was chosen in order to achieve the highest possible wavelength resolution and intensity. The reflex position on the film, placed into the H-beam, could be used to calibrate the wavelength, and harmonics were suppressed by the Bragg-Laue combination. The result of the measurement is plotted in Fig. 9. It shows a smooth wavelength dependence of f' on the long wavelength side of λ_K and reflects the well-known EXAFS structure of the absorption spectrum for $\lambda < \lambda_K$. Here the intermediate electron state is modulated close to the edge by the conduction bands of the solid and can further out be interpreted by taking the backscattering from neighbouring atoms into account. The arrows in Fig. 9 illustrate the correspondence of the f' structure to the minima (below the curve) and maxima (above the curve) of the absorption spectrum measured by Cauchois and Manescu (1950).

The errors in the above f' measurement were mostly determined by inhomogeneities of film shrinkage and sample thickness. Here the use of detectors and the calibration of the thickness with a wavelength far away from the absorption edge (Cusatis and Hart (1975)) for example with $\lambda/2$ will establish a standard method for precise f' determination.

High intensity, continuous wavelength spectrum and high collimination are the decisive advantages of synchrotron radiation in this application.

5.2 Three-beam case interferometer

The setup of the three-beam case interferometer used by Graeff and Bonse (1977) at DESY is shown in Fig.10. A 220 germanium groove has been selected to get away from the spot hit by the primary beam and to suppress the higher orders. This is done by using the method discussed in chapter 4 and combining two materials with different electronical densities (see equations (2) and (4)) in this case the germanium groove with the (440, 404) silicon interferometer.

The ray course of the interferometer is sketched in Fig. 10. All rays are coplanar with the incident beam because the right wavelength can be chosen from the continuous spectrum. The choice of this coplanar case was crucial for the operation of the interferometer because the temporal coherence length $l_c = \lambda^2/\Delta\lambda$ is determined by the wavelength resolution. If the incoming beam is tilted by an angle η against the ray plane shown in Fig. 10 it follows from Braggs law and geometry that $\Delta\lambda/\lambda \approx \eta^2/2$, if the divergence is kept constant. The coherence length thus decreases. Of course this is also true, if the divergence perpendicular to the reflection plane increases.

A large coherence length is necessary in this experiment because the surface roughness decreases the temporal coherence. Graeff (1976) estimated that the vertical

divergence of synchrotron X-radiation corresponds for $\lambda = 1.66$ Å to a coherence length $l_c \approx 15 - 30$ µm which is enough to reflect consecutively from several Bragg mirrors each with a surface roughness of about 0.2 µm. A horizontal reflection plane was used and wavelength tunability and high collimation were the most important parameters of synchrotron X-radiation.

Acknowledgement

The author likes to thank Prof. Dr. U. Bonse for many discussions about the above topic.

Bauspieß W., Bonse U. & Graeff W. (1976). J. Appl. Cryst. 9, 68

Bonse U. & Materlik G. (1975 a). Anomalous Scattering, edited by S. Ramaseshan & S.C. Abrahams, pp. 107 - 109. Kopenhagen: Munksgaard

Bonse U. & Materlik G. (1975 b). Acta. Cryst. A 31 S3, 232

Bonse U. & Materlik G. (1976). Z. Physik B 24, 189

Bonse U., Materlik G. & Schröder W. (1976). J. Appl. Cryst. 9, 223

Borrmann G. (1955). Z. Kristallogr., Mineralog., Petrogr. 106, 109

Cole H., Chambers F.W. & Wood C.G. (1961). J. Appl. Phys. 32, 1942

Ceuchois Y. & Manescu T. (1950). J. chim. phys. Physico-Chim., Biol. 47, 892

Cusatis C. & Hart M. (1975). Anomalous Scattering, edited by S. Ramaseshan & S.C. Abrahams, pp. 57 - 68. Kopenhagen: Munksgaard

Deslattes R.D. (1968). Appl. Phys. Letters 12, 133

Graeff W. (1976). PhD Thesis, Univ. of Dortmund

Graeff W. & Bonse U. (1977). Z. Physik B 27,19

Green K. (1975). BNL. Report 50595, Brookhaven National Laboratory, New York

Hart M. (1975). Proc. R. Soc. A 346, 1

Hastings J.B. (1977). J. Appl. Phys. 48, 1576

Indenbom V.L., Slobodetskii I.S. & Truni K.G. (1975). Sov. Phys. JETP 39, 542

Kunz C. (1976). Optical Properties of Solids, edited by B.O. Seraphin, pp. 477 - 553. Amsterdam: North-Holland

Materlik G. (1975). PhD Thesis, Univ. of Dortmund

Materlik G. & Kostroun V.O. (1978). to be published

Pianetta P. & Lindau I. (1977). J. of Electr. Spectr. and Rel. Phenom. 11, 13

Zachariasen W.H. (1967). Theory of X-ray Diffraction in Crystals. New York: Dover

Fig. 1 Interferometric setup. S Stationary slit; MO Monochromator; G Goniometer; M Monitor counter; IF Interferometer; C Counter; F Film.

Fig. 2 Channel cut monochromator with lead shielding (lead cover is removed).

Fig. 3 a) Interferometer mount for vertical reflection plane. St Steel.
b) Built-in moiré.

Fig. 4 a) Intensity distribution of synchrotron radiation as a function of the inclination angle Ψ to the orbit plane for $\lambda = 1.5$ Å. $P_{\parallel}$, $P_{\perp}$ for the electrical vector parallel and perpendicular to the orbit respectively.
b) Typical phase space ellipse for DORIS at 3 GeV electron energy .
(For description see text.)

Fig. 5 a,b) Fringe moirés and densitometer traces along the indicated ways (arrows) for two different electron beam optics of DESY. S optical density. Note the contrast change and the similarity between S and $P_{\perp}$

Fig. 6 Synchrotron radiation intensity of DESY in a slit 29 m away from the tangent point, 0.5 mm wide and 7 mm high for different electron end-energies 4, 5, 6, 6.5 and 7.2 GeV for the curves 1, 2, 3, 4 and 5 respectively. Beam current is 10 mA. $\Delta\lambda = 10^{-3}$ Å. (R), (C) corresponding intensities from a 30 kW Rigaku Denki rotating anode and a conventional 1.5 kW X-ray tube.

Fig. 7 Bragg case single crystal reflection curves.

Fig. 8 Wedge moirés for reflexions $\lambda = 1.5$ Å, $\lambda/2$ and $\lambda/3$. H-beam left column, O-beam right column.

Fig. 9 Measured f' dependence of nickel on either side of the K absorption edge. Arrows indicate the structure measured in absorption: arrows above the curves give the positions of the maxima, arrows below those of the minima.

Fig. 10 Setup with three-beam case interferometer and ray path.
PP Photographic plate.

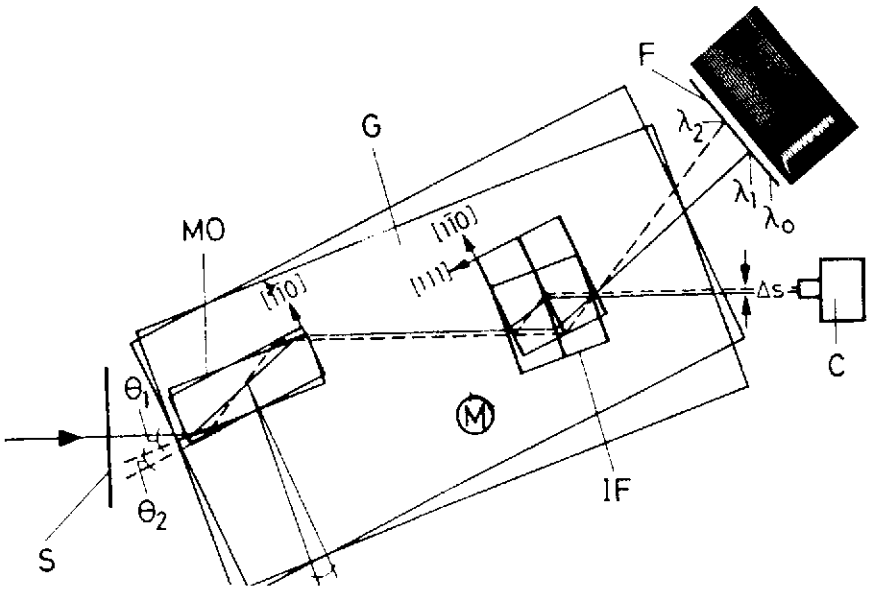
F
G
MO
λ_2
λ_1
λ_o
$[\bar{1}10]$
$[111]$
$[1\bar{1}0]$
Δs
C
θ_1
M
IF
θ_2
S

Fig. 1

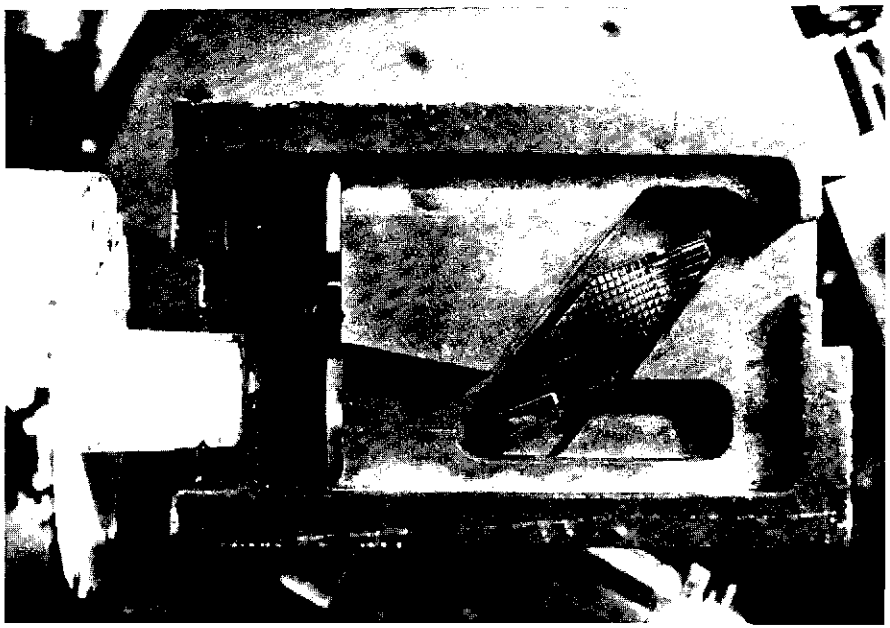

Fig. 2

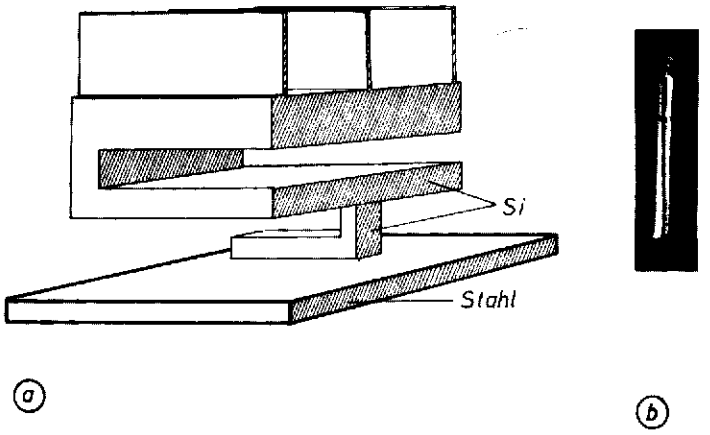

Fig. 3

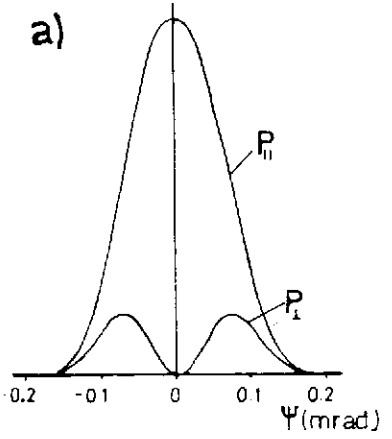

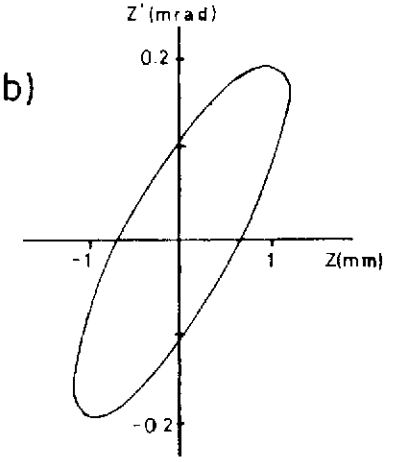

Fig. 4

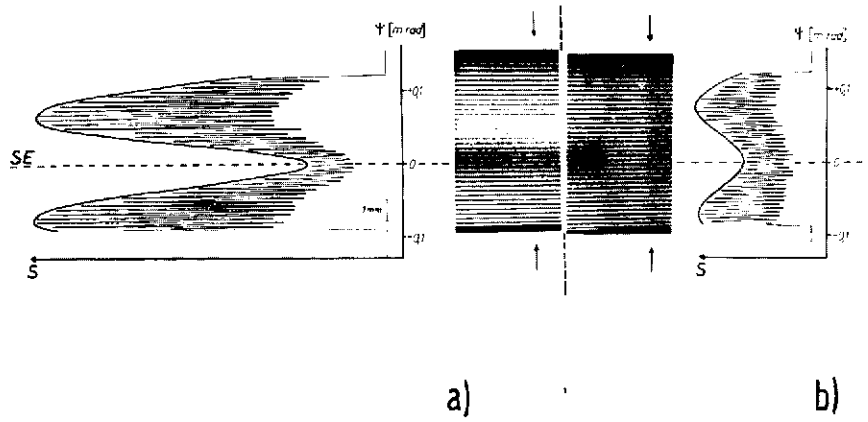

Fig. 5

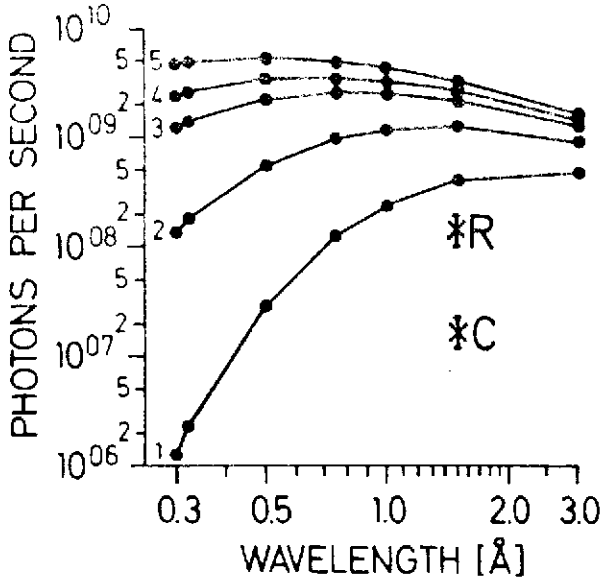

Fig. 6

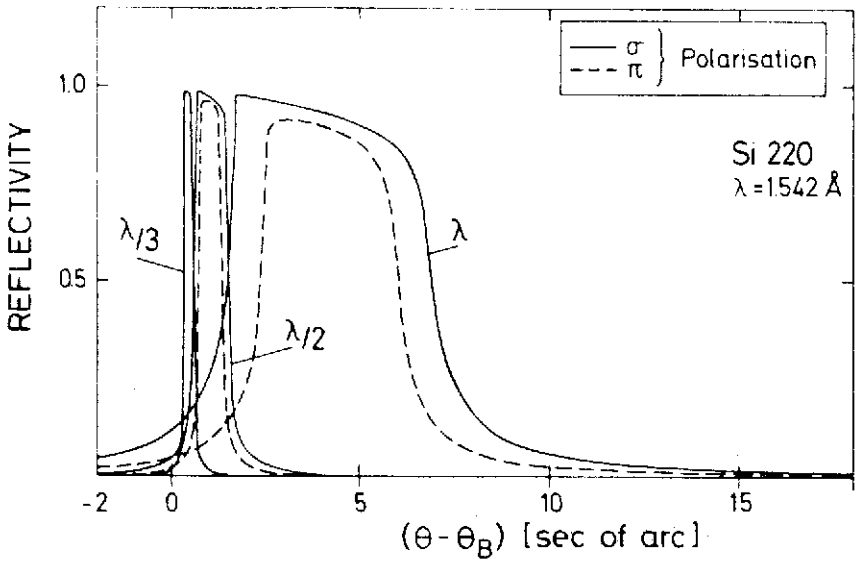
REFLECTIVITY
1.0
0.5
σ
π
Polarisation
Si 220
λ = 1.542 Å
λ/3
λ/2
λ
-2
0
5
10
15
(θ - θB) [sec of arc]

Fig. 7

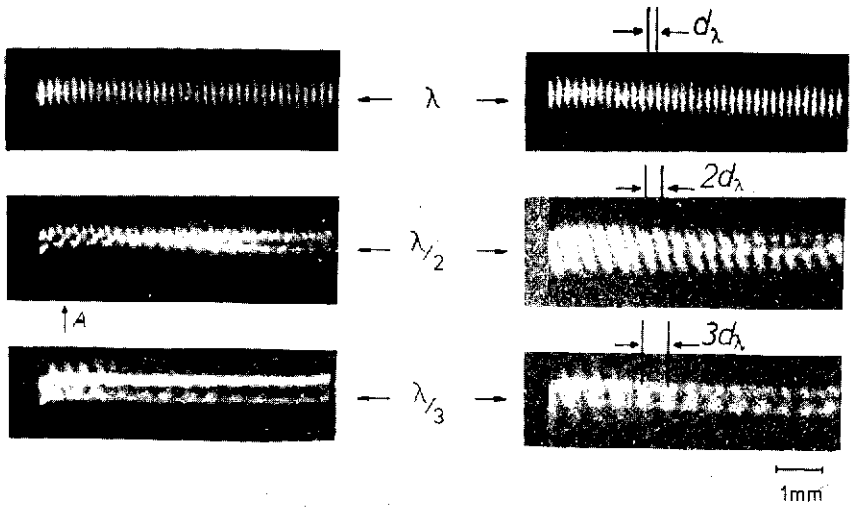
λ
λ/2
λ/3
A
dλ
2dλ
3dλ
1mm

Fig. 8

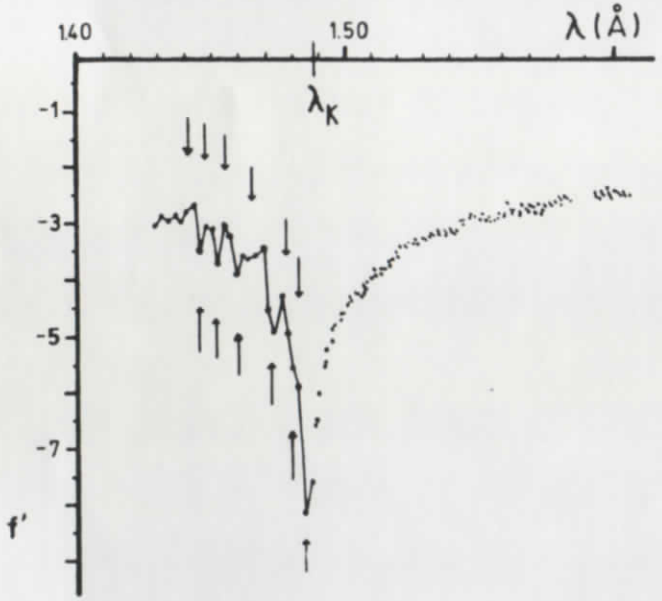
1.40
1.50
λ (Å)
λK
-1
-3
-5
-7
f'

Fig. 9

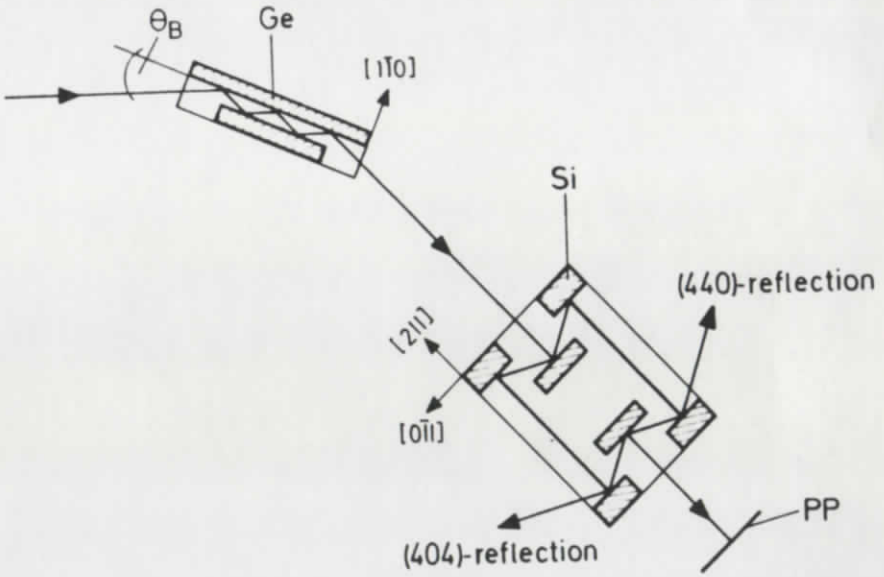
θB
Ge
[1$\bar{1}$0]
Si
(440)-reflection
[211]
[0$\bar{1}$1]
PP
(404)-reflection

Fig. 10